Multi-axial integrated optics solution for POPS, a 2^{nd}-generation VLTI fringe tracker

Nassima Tarmoul[a], François Hénault[a], Denis Mourard[a], Jean-Baptiste Le Bouquin[b], Laurent Jocou[b], Pierre Kern[b], Jean Philippe Berger[c], Olivier Absil[d]

[a]Université de Nice Sophia, Observatoire de la Côte d'Azur, CNRS, Laboratoire H. FIZEAU, UMR 6525, Avenue Nicolas Copernic, 06130 Grasse, France;
[b]Université Joseph-Fourier, CNRS, Laboratoire d'Astrophysique de Grenoble, UMR 5571, BP 53, 38041 Grenoble, France;
[c]European Southern Observatory, Vitacura, Chile;
[d]Université de Liège, Institut d'Astrophysique et de Géophysique, 17 Allée du Six Août, B-4000 Liège - Belgium

ABSTRACT

POPS (Planar Optical Phase Sensor) is a second-generation fringe tracker for the Very Large Telescope Interferometer (VLTI), intended to simultaneously measure the cophasing and coherencing errors of up to six Unit Telescopes (UT) or Auxiliary Telescopes (AT) in real time. The most promising concepts are probably based on the utilization of Integrated Optics (IO) components, and were the scope of a Phase A study led by Observatoire de Grenoble (LAOG). Herein is described a tentative design built around a multi-axial IO chip whose fringes are dispersed downstream on a detector array, and a Chromatic Phase Diversity algorithm presented in another paper of this conference[1] . We depict the foreseen opto-mechanical, detection and software implementations, and provide numerical results from a realistic simulation model in terms of group and phase delay measurement accuracy and limiting magnitudes in the K band. The ultimate performance of the method is discussed and compared with the original 2^{nd} generation VLTI fringe tracker requirements.

Keywords: Phased optical arrays, Phase retrieval, Fringe tracker, Integrated Optics

1. INTRODUCTION

In the perspective of the realization of future, second generation instruments of the Very Large Telescope Interferometer (VLTI) such as GRAVITY, MATISSE and VSI beam combiners, European Southern Observatory (ESO) is currently planning to install a new, 2^{nd} Generation Fringe Tracker (2GFT) at the VLTI focus, being able to simultaneously measure cophasing (or phase delay) and coherencing (or group delay) errors of up to six Unit Telescopes (UT) or Auxiliary Telescopes (AT) in real time. Following a Call for Proposals on late 2008, several institutes have been selected by ESO for a Phase A study aiming at defining the baseline design of the future fringe tracker. Among them, a Consortium composed of Laboratoire d'Astrophysique de Grenoble (LAOG, Grenoble, France), Laboratoire Hippolyte Fizeau (Grasse, France) and Institut d'Astrophysique et de Géophysique de Liège (IAGL, Liège, Belgium) decided to concentrate their main effort on designs based on the utilization of Integrated Optics (IO) components. Indeed, experience shows that classical solutions in bulk optics tend to increase in terms of complexity, cost, mass, volume and sensitivity to thermal environment as more and more interferometric arms are to be combined together. The selected IO technical solution was named POPS, an acronym that stands for "Planar Optical Phase Sensor". In this framework, we had the responsibility, at Laboratoire H. Fizeau, to develop a concept for real-time fringe tracking with a multi-axial Integrated Optics Combiner (IOC) and a dispersed fringes technique[2,3] and to assess the actual performances.

The major technical requirements for 2GFT[4] are summarized in Table 1. They are all applicable to sky objects of magnitudes 7 and 10 in the K band when ATs and UTs are respectively used, under typical seeing

Further author information: (Send correspondence to François Hénault)
E-mail: Francois.Henault@obs-azur.fr, Telephone: +33 (0)4 93 40 53 58

SPECIFICATIONS	Phase Delay mode	Group Delay mode
Measurement noise	<100nm RMS	800nm RMS
Total signal delivery time	600μs	10ms
Detector Integration Time	500μs	5ms
Linearity	10% over $\pm$1.05μm range	20% over $\pm$6μm range
Detector pixel size	18*18μm	
Read time	20μs/pixel	
Read-Out Noise (RON)	<15 electrons/pixel (goal 10)	
Dark current	<0.01 electrons/pixel/sec	

Table 1. Major technical requirements for 2GFT.

conditions at Cerro Paranal, Chile: 0.8 arcsec on-sky and a 3 ms coherence time. The Optical Path Differences (OPDs) to be measured typically lay in the range $\pm$ 6μm. In addition, emphasis was put on a few specific issues, such as association between telescopes of different sizes (*i.e.* UTs and ATs), impact of unequal source visibilities on varying VLTI baselines, or effects of polarization. The Table also lists some practical constraints that are related to the choice of the detector array, which is a Hawaii 2RG CCD matrix manufactured by Rockwell Scientific.

2. DESCRIPTION OF THE DESIGN

2.1 General description of the multi-axial IO solution using the Chromatic Phase Diversity method

The proposed design is presented in Fig. 1 and looks rather simple, at least from optical and mechanical point of views, which should ensure a good stability compatible with IO components performance: let us consider an ensemble of N VLT telescopes that are to be phased together. The optical beams reflected from each telescope are conveyed (*e.g.* by means of optical fibers) and injected into a multi-axial IO beam combiner generating a polychromatic fringe pattern at its exit face. This IOC is set at the entrance slit of a low dispersion spectrograph equipped with a small angle prism as shown in the Figure. The slit is imaged on a CCD matrix at L different wavelengths l, with 1 $\leq$l$\leq$L. On-chip binning may be employed, thus enabling to integrate the spectrally dispersed fringes on spectral channels of variable widths $\delta\lambda_1$(1 $\leq$l$\leq$L). This principle allows reconfiguring rapidly the main measurement parameters, which are the integer number L and the λ_1 and $\delta\lambda_1$ sets of values, hence to optimize them so as to minimize piston measurement errors on each telescope. The study is herein restricted to the case when L = 3, a configuration leading to satisfactory results in terms of both piston measurement accuracy and capture range (an alternative concept for actual implementation is based on the use of the series of dichroic plates aiming at selecting the three spectral bands as in the design described in the SIRIUS paper[1] of this conference).

Given three linear interferograms I'(x', λ_1), I'(x', λ_2) and I'(x', λ_3) being acquired simultaneously at the output of the IOC for three different reference wavelengths λ_1, λ_2 and λ_3, the rest of the OPD measurement method essentially consists in data processing, whose principle is roughly summarized below. It must be emphasized that all the employed algorithms are very fast in terms of computing time (see Sec. 2.4) and therefore suitable for real-time applications as is required for a ground fringe tracker.

1. Each linear interferogram I'(x', λ) undergoes an inverse Fourier Transformation providing access to the complex Optical Transfer Function (OTF) of the IOC sub-pupil arrangement (here and in the remainder of the text the wavelength subscript "l" is omitted for the sake of simplicity):

$$OTF(x,\lambda) = FT^{-1}[I'(x',\lambda)] \tag{1}$$

2. The IOC Modulation Transfer Function MTF(x, λ) - that is just the OTF modulus - is mapped along the X-axis in order to detect its first $\frac{N(N-1)}{2}$ local maxima. For non-redundant, single-mode channels configurations such as depicted in Fig. 2 and a judicious choice of geometrical parameters, all the OTF peaks are well separated spatially. Phases of the averaged OTFs may then be estimated over $\frac{N(N-1)}{2}$ sub-areas centered on the theoretical locations of the MTF peaks.

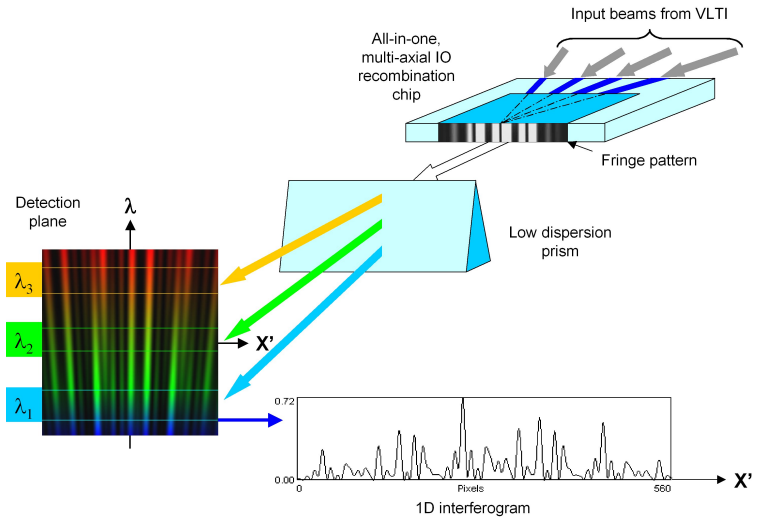

Figure 1. General principle of the multi-axial fringe sensor.

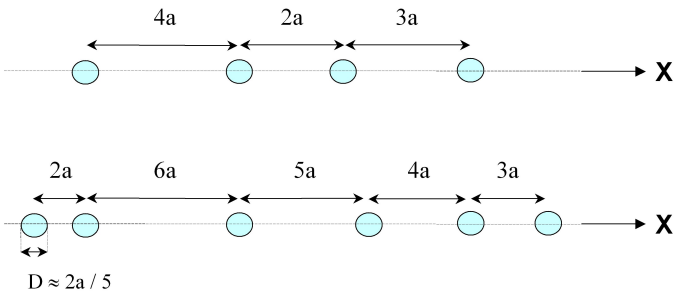

Figure 2. Non-redundant channels configurations for combining four and six telescopes (resp. top and bottom panels).

3. The phase differences $[\phi_n\text{-}\ \phi_{n'},\ \lambda]$ for the three selected wavelengths and all couples (n, n') of telescopes (with $1 \leq n < n' \leq N$) are extracted from OTF(x, λ) on their associated MTF peaks, using the formula*:

$$[\phi_n - \phi_{n'}, \lambda] = \arctan \frac{Im[OTF(x,\lambda)]}{Real[OTF(x,\lambda)]} \tag{2}$$

   Im[] and Real[] respectively standing for imaginary and real parts of a complex function.

4. Phase differences values $[\phi_n\text{-}\ \phi_{n'},\ \lambda]$ are finally transferred to the Chromatic Phase Diversity algorithm (see Sec. 2.3), which reconstructs and unwraps all the piston errors p_n affecting the N VLTI telescopes.

In the following sections is provided additional information about the multi-axial IOC and fringes formation (Sec. 2.2), CPD algorithm (Sec. 2.3), and an end-to-end numerical model simulating the whole piston measurement process (Sec. 2.4).

2.2 Multi-axial Integrated Optics component

From multiple optical solutions using IO technology suitable for 2GFT, the presented design makes use of multi-axial beam combiners. Also known as "all-in-one combiners", the latter have been envisaged for either interferometric imaging or fringe-tracking purposes since a dozen years[5,6,7,8,9] . Referring to these previous studies, a multi-axial IOC looks like a thin sheet of optical glass of typically 40 x 20 mm dimensions, in which

*In practice we use an intrinsic function returning phase values over the range $[-\pi, +\pi]$.

planar Single-Mode Waveguides (SMWs) have been buried by means of photo-masking and ion exchange or etching techniques. In the multi-axial design, SMW directions are converging to a common point O' where all the transported Gaussian beams can interfere together. This interference occurs within a tapered area spreading in the XZ plane of the IO chip from a reference point O, as presented in Fig. 3. Denoting L=‖OO'‖ the depth of the tapered area, the width of the output interferogram along the X'-axis will be equal to 2 Lα_x, where α_x is the exit numerical aperture of an individual SMW. The width D'$_y$ of the interferogram along the orthogonal direction Y' remains comparable to the SMW core diameter D due to the single-mode confinement along that direction. Hence approximate relationships defining the created interferograms I'(x', λ) are provided below.

2.2.1 Monochromatic interferogram

A simplified expression of the theoretical monochromatic interferogram at the output of the IOC is:

$$I'(x',\lambda) = \exp[-(\frac{x'}{L\alpha_x})^2] \sum_{n'=1}^{N} \sum_{n=1,n<n'}^{N} cos[\frac{2\pi\xi_{n,n'}(x')}{\lambda}] \tag{3}$$

with global OPD $\xi_{n,n'}(x')$ between a couple (n, n') of different telescopes being equal to:

$$\xi_{n,n'}(x') = \frac{x'(x_{n'} - x_n)}{L} + (p_{n'} - p_n) \tag{4}$$

with 1≤n≤N and where the parameters x_n are the Cartesian coordinates of all output waveguides along the OX axis, and p_n are the original piston errors to be measured.

2.2.2 Effect of finite spectral bandwidth

In principle, all monochromatic interferograms should be numerically integrated over their useful spectral channels of width $\delta\lambda$ and centred on their reference wavelength λ_0:

$$I_{\delta\lambda}(x',\lambda_0) = \int_{\lambda_0-\frac{\delta\lambda}{2}}^{\lambda_0+\frac{\delta\lambda}{2}} I(x',\lambda)d\lambda \tag{5}$$

These computations, however, can be considerably simplified and speeded up when considering that in practice $\delta\lambda$ will be sensibly smaller than λ_0, hence the approximation $\frac{1}{\lambda} \approx \frac{1}{\lambda_0} - \frac{\Delta\lambda}{\lambda_0^2}$ holds and changing variable λ to $\Delta\lambda$ into integral of Eq. (5) readily leads to an approximate expression for $I_{\delta\lambda}(x',\lambda_0)$:

$$I_{\delta\lambda}(x',\lambda_0) \approx \exp[-(\frac{x'}{L\alpha_x})^2] \sum_{n'=1}^{N} \sum_{n=1,n<n'}^{N} cos[\frac{2\pi\xi_{n,n'}(x')}{\lambda}]\text{sinc}[\frac{\pi\xi_{n,n'}(x')\delta\lambda}{\lambda_0^2}] \tag{6}$$

sinc(u) being the sine cardinal function equal to $\frac{\sin(u)}{u}$.

2.2.3 Radiometric normalisation

To be usable, Eq. (6) must finally be multiplied by an irradiance factor E_0 being equal to:

$$E_0 = N_P/(\pi L\alpha_x D'_y) \tag{7}$$

where N_P is the total number of photons/second/m^2 available per spectral channel, originating from one single telescope and taking into account the global optical and radiometric efficiencies of the atmosphere, VLTI facility, POPS optical design and detector quantum efficiency. For the K band, we use the approximate formula:

$$N_P = 4.5310^9 A_T \eta\delta\lambda 10^{-m/2.5} \tag{8}$$

where A_T is the collecting area of one telescope in m^2, η is the global radiometric efficiency and m the magnitude of the target star, the spectral bandwidth $\delta\lambda$ being expressed in terms of μm.

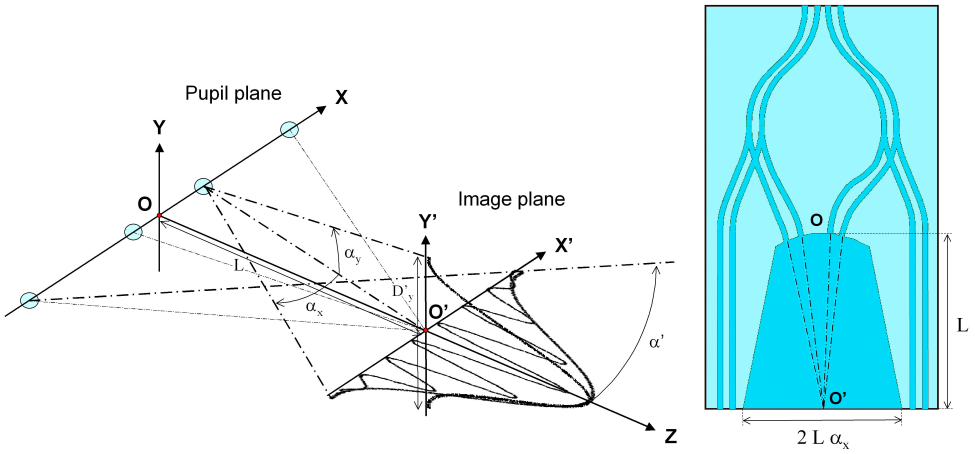

Figure 3. Main geometrical parameter of multi-axial combination area.

2.3 Chromatic Phase Diversity algorithm

Classical phase diversity methods are based on the comparison between two images of the same object obtained simultaneously. These images are linked to each other by an *a priori* known relation such as defocus[10] or piston added into a reference sub-pupil.[11] Here is employed a "chromatic phase diversity" method originally intended for cophasing future large interferometric arrays.[12] Indeed, comparing in the same plane several monochromatic images obtained at chosen wavelengths, the absolute piston p_n of each aperture can be determined if the phase relation linking the analyzed images is known *a priori*. The use of several different wavelengths allows lifting the well-known 2π ambiguities of phase measurements as shown by Lofdahl and Eriksson.[13] The implemented CPD algorithm enables to extract the piston value of each sub-pupil compared to a reference sub-pupil of the interferometer. The principle consists in taking advantage of the relationship between the wavelength and the wave's phase state. The piston value of each sub-aperture can therefore be extracted and make the cophasing possible. Indeed, the differential piston values $[p_n - p_{n'}, \lambda]$ are related to the phase differences values $[\phi_n - \phi_{n'}, \lambda]$ as follow:

$$[p_n - p_{n'}, \lambda] = \frac{\lambda \cdot [\phi_n - \phi_{n'}, \lambda]}{2\pi} \pm k\lambda \tag{9}$$

with k a relative integer describing the 2π uncertainty on the phase measurement and defining the capture range in number of wavelength where the piston should be present. The method is detailed in the paper presenting the CPD method implemented on the SIRIUS testbench.[1]

The first step of the CPD algorithm consists in comparing the possible piston values $[p_n - p_{n'}, \lambda_1]$, $[p_n - p_{n'}, \lambda_2]$, $[p_n - p_{n'}, \lambda_3]$ within the capture range $[\frac{-k\lambda}{2}, \frac{+k\lambda}{2}]$, as shown on Fig. 4:

Considering one baseline, comparing the potential piston values for λ_1, λ_2 and λ_3 makes it possible to recover the sought piston value of each baseline. φ_1, φ_2, and φ_3 correspond to the extracted phases at respectively λ_1, λ_2 and λ_3 (see Eq (2)). The absolute value of the pistons is not important for the cophasing because we are only looking for differential pistons. Thus one sub-pupil is identified as reference and the N-1 differential pistons could be determined on the N-1 baselines formed with this reference sub-pupil. Depending of the parameter ε used for the precision of the comparison between wavelengths, the algorithm may provide one or more solutions for the piston on the N-1 sub-pupils. So the last step of the algorithm is to reprocess the previous comparison with an other choice of ε or to test these different solutions with respect to the differential pistons measured on all the other baselines. Finally, one gets the N-1 differential pistons needed for the cophasing of the array.

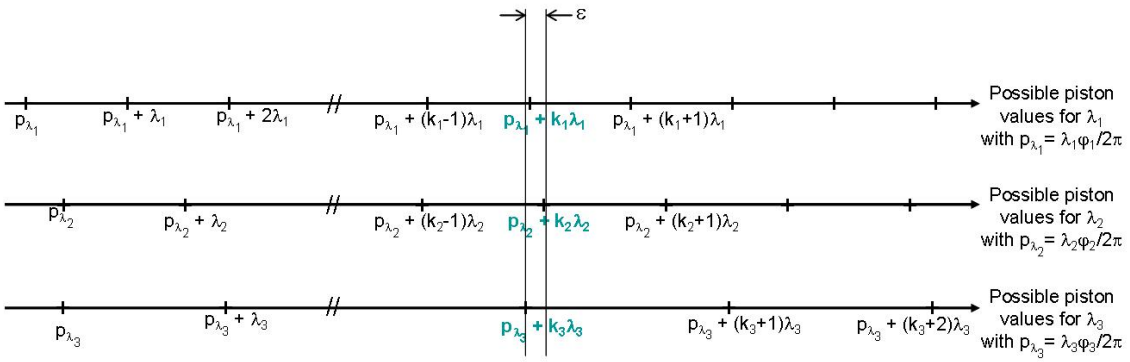

Figure 4. Principle of the algorithm.

τ	Detector Integration Time (DIT) in seconds
s_p	Pixel sensing area in m^2
N_B	Total number of photons/second/m^2 originating from thermal background
n_p	Total number of useful pixels along the X'-axis
RON	Read-out noise expressed in terms of electrons/pixel
d	Dark current noise expressed in terms of electrons/pixel/second

Table 2. Main parameters of the detection unit.

2.4 Numerical model

In order to assess the performance of the presented optical design and algorithms, we have developed an end-to-end numerical model taking into account most of the physical parameters intervening either in the fringe formation process or in the data reduction procedure, until phase differences are finally extracted and translated in terms of piston measurement errors. A simplified flow-chart of the numerical model is provided in Fig. 5. In addition to various IOC parameters described in Sec. 2.2, the code also allows to introduce the coupling ratios ρ_n from each telescope into the SMWs as well as their fluctuations with time $\delta\rho_n$. It must be noted that these parameters that are introduced as weighting factors $\rho_n\rho_{n'}$ into Eq. (6)) can also be used when studying the case of combining telescopes of different diameters (*i.e.* ATs with UTs, see Sec. 3.2.2). Likewise, visibility factors $V_{n,n'}$ can be added in the same relationship to take sky objects being partly resolved by some of the VLTI baselines into account. Finally, detection noises δI(x') are added to the ideal estimated interferograms $I_{\delta\lambda}(x', \lambda)$:

$$I'(x', \lambda) = I_{\delta\lambda}(x', \lambda)\tau s_p + \delta I(x') \tag{10}$$

where δI(x') incorporates shot noise from the target star, thermal background and detector read-out and dark current noises, added in quadratic sense. The definition of all parameters appearing in Eq. 6 and in Eq. 11 is summarized in Table 3.

$$\delta I(x') = [(I_{\delta\lambda}(x', \lambda) + N_B)\tau s_p + n_p(RON^2 + d\tau)]^{1/2} \tag{11}$$

The resulting numerical model has proved to be very efficient since the whole computations are carried out in less than one second on a 4-years old laptop computer using IDL script language. It was checked that the global computing time is essentially driven by the employed Fourier transform procedure, since all other mathematical operations including CPD algorithm are performed in less than one millisecond. Typical examples of graphic outputs showing the acquired interferograms, their MTFs and phases extracted from the complex OTFs are reproduced in Fig. 6 for the four telescopes case.

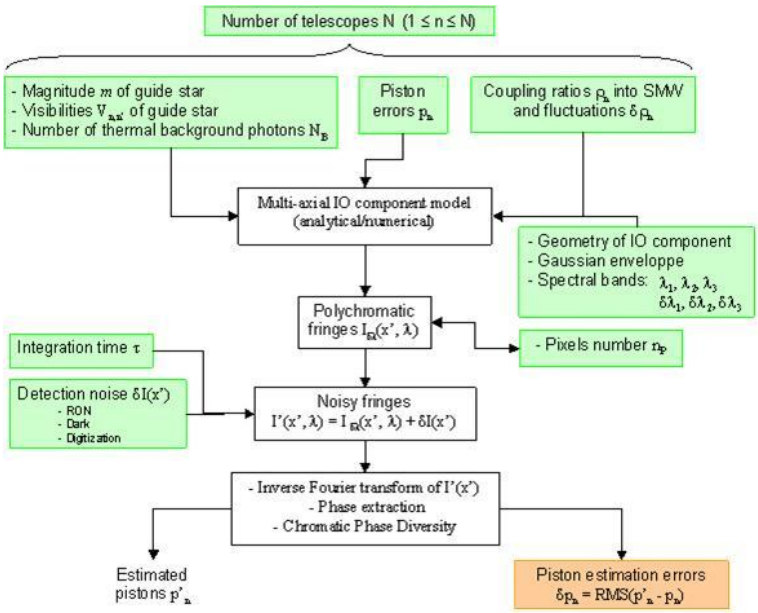

Figure 5. Flow-chart of the numerical model.

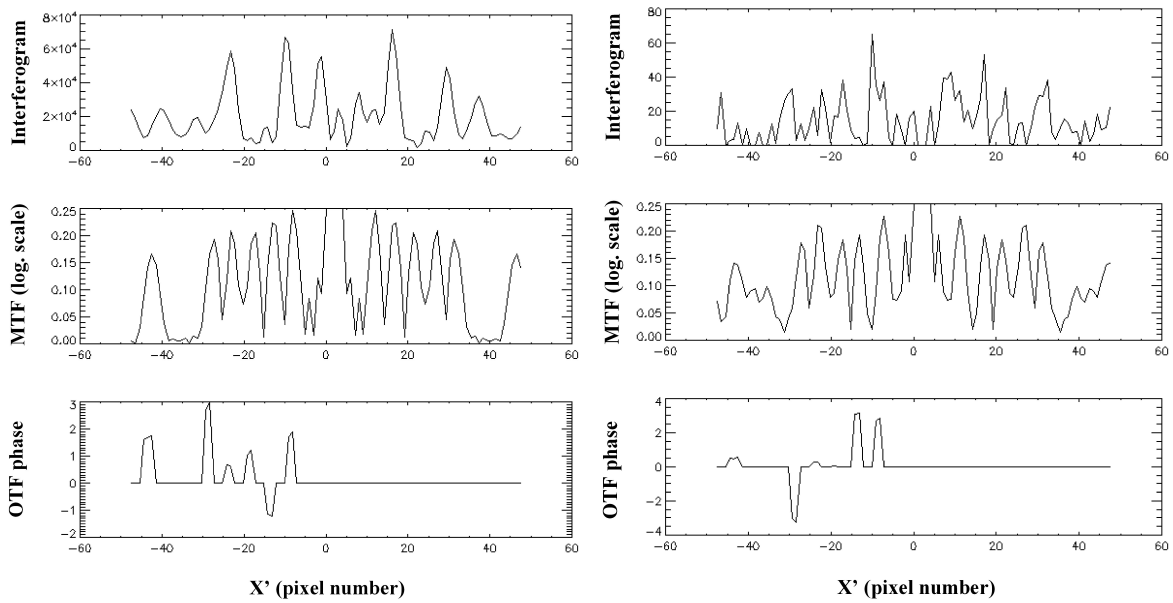

Figure 6. Examples of outputs of the numerical model in the cases of four telescopes of high and low SNR (respectively left and right figure).

PARAMETERS	4 telescopes	6 telescopes
Central wavelengths	2., 2.2 and 2.4 μm	
Channel spectral widths	0.20 μm	
Thermal background N_B	4220	1670
Spectrograph entrance aperture (1/2α')	F/4.9	F/7.9
Total number of pixels n_p	95	255
Number of pixels per fringe	4.80	4.64
SMW core diameter D	10 μm	
Minimal spacing between SMW cores 2a	50 μm	
SMW exit aperture α_x	0.12 radians	
Length of tapered area L	8 mm	
height of tapered area D'$_y$	8.9 μm	

Table 3. Summary of main IOC input parameters.

3. ACHIEVABLE PERFORMANCE

Using the end-to-end numerical model described in the previous section, we carried out a preliminary sensitivity analysis providing first estimates of the achievable fringe tracking errors when associating a multi-axial IOC component with dispersed fringes principle and the CPD algorithm. All the entrance parameters are summarized in the Table 3 below, and also in Table 1 for what concerns detector characteristics. The numerical values of some of the parameters in Table 3 result from a preliminary optimization, where we sought in particular to minimize the number of needed pixels n_P along the X'-axis (from -Lαx to +Lαx), and consequently the read-out noise, while maintaining OPD measurement errors typically below 20 nm. It finally turned out that the spectral bandwidths can be set to their maximal values of 200 nm for both the 4T and 6T cases (which corresponds to 9% for a reference wavelength of 2.2μm in the K band), and that minimal pixels numbers are 95 and 255 respectively, which corresponds to a pixel per fringe sampling ratio slightly inferior to 5.

In the following sections, the fringe tracking errors are principally expressed in terms of RMS measurement accuracy δp_n of the random piston errors introduced on each telescope. Success ratios are also provided, deduced from Monte-Carlo analysis of typically 100 different cases. Failures in piston retrieval usually occur when one or more phase differences $[\phi_n - \phi_{n'}, \lambda]$ could not be extracted from the complex OTFs for one wavelength at least. We only consider four ATs of 1.8-m diameter in the for 4T case, and in the 6T cases we consider firstly the case with 6 ATs and secondly the case with 2 UTs of 8-m diameter coupled with 4 ATs. A global radiometric efficiency η of 0.05 is assumed for the VLTI and detection system. The influence of various parameters such as magnitude of the target star, DIT or RON is then studied in the following paragraphs.

3.1 Coupling four Auxiliary Telescopes

In this section is only considered the case when four Auxiliary Telescopes (ATs) are coupled together. Sec. 3.1.1 and 3.1.2 respectively deals with the influence of Detector Integration Time (DIT) and Read-out Noise (RON).

3.1.1 Influence of Detector Integration Time (DIT)

For a magnitude of the target star ranging from 0 to 10 in the K band, we have plot the achieved piston measurement accuracy in terms of nanometers for three different DIT values, namely:

- DIT = 0.5 msec, which is the initial requirement for cophasing, or phase delay mode (piston errors comprised between -$\frac{\lambda_0}{2}$ and +$\frac{\lambda_0}{2}$, see Table 1).
- DIT = 5 msec for coherencing, or group delay mode, assuming piston errors in the range [-3λ_0, +3λ_0].
- DIT = 50 msec, a case when excellent conditions of observation are encountered on the telescope site.

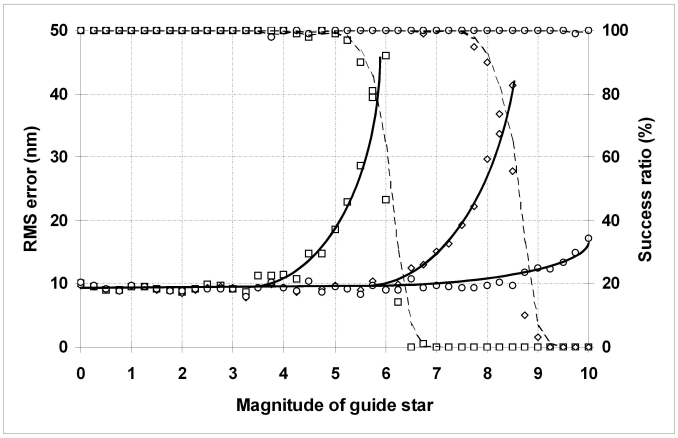

Figure 7. Phasing error (solid lines) and success ratio (dashed lines) as functions of magnitude of the target star and detector integration time with DIT = 0.5 ms (squares), 5 ms (losanges) and 50 ms (circles) and RON = 10 electrons/pixel.

The measurement accuracy is computed in RMS sense over 100 sets of randomly generated pistons errors. The target star is assumed perfectly unresolved so that all visibility coefficients $V_{nn'}$ of the interference terms are taken equal to 1. In these conditions the numerical results are displayed graphically in Fig. 7, showing that the measurement error is around 10 nm RMS and stays remarkably stable over a wide range of magnitudes, until the achieved success ratio suddenly collapses from 100% down to 0% in less than one magnitude. In that region, RMS errors increase very rapidly up to 40 nm until unacceptable success ratios are attained (*e.g.* lower than 90%). Such behavior typically occurs in low photon regime when the Signal-to-Noise Ratio (SNR) of the interferogram becomes inferior to 10. Hence it may be concluded that the actual piston measurement accuracy mostly depend on some design characteristics of the fringe tracker such as the required number of pixels n_P and the channels spectral bandwidth $\delta\lambda$ on the one hand, and that, on the other hand, the method rapidly breaks of when radiometric conditions become too unfavorable. Another interesting property of the multi-axial design is the fact that we did not observe significant differences between the phase and group delay modes, the OPD measurement errors staying comparable. Consequently, the method shows identical performance for both cophasing and coherencing operations and is naturally immune to phase jumps in the considered piston error domain.

The curves in Fig. 7 finally demonstrate that limiting magnitudes of 5, 8 and 11 could be attained for DITs respectively equal to 0.5, 5 and 50 msec. Hence 2GFT requirements are not fulfilled in phase delay mode, but this mostly originates from the very short DIT imposed by the required number of pixels n_P and the read-out time of the Hawaii 2RG detector. In group delay mode, however, the 2GFT requirements seems attainable. In both cases the measurement noise and linearity requirements of Table 1 are easily met.

3.1.2 Influence of Read-out Noise (RON)

The effects of detector read-out noise on POPS limiting magnitudes are illustrated on Fig. 8. With respect to a reference case when RON = 10 electrons/pixel (which is the design goal of the Hawaii 2RG camera), one can see that an improved value of RON = 5 electrons/pixel results in a half-magnitude gain. Conversely, a degraded value of 20 electrons/pixel induces a one magnitude loss. We also noticed that RON and photon noise are the dominant sources of errors, since the influence of dark current, thermal background and digitization errors on 12-bits was found negligible.

3.2 Coupling six VLT telescopes

In this section are considered two cases where six VLT telescopes are combined: first when 6 ATs are coupled together (Sec. 3.2.1), then when 2 UTs are combined with 4 ATs (Sec. 3.2.2).

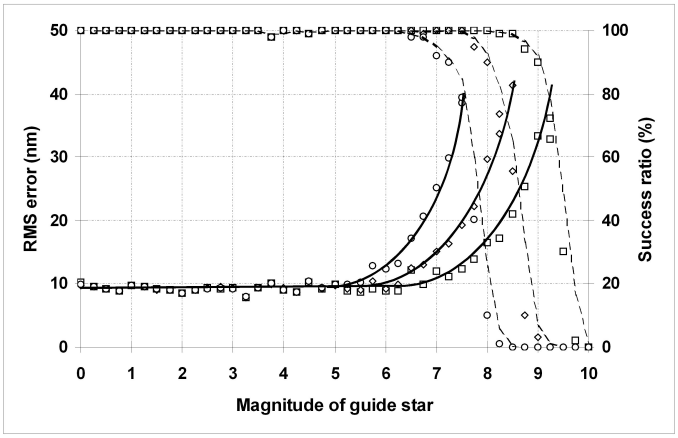

Figure 8. Same diagram as in Fig. 7 with DIT = 5 ms and RON = 5 (squares), 10 (losanges) and 20 electrons/pixel (circles).

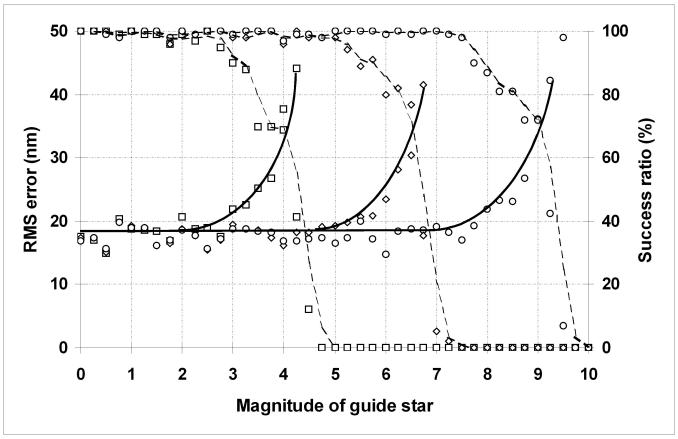

Figure 9. Same diagram as in Fig. 7 in the case of six telescopes (ATs) with DIT = 0.5 ms (squares), 5 ms (losanges) and 50 ms (circles) and RON = 10 electrons/pixel.

3.2.1 Coupling 6 ATs

Excepting the telescope number, numerical simulations have been carried out with the same parameters than in sec. 3.1.1, and their results are displayed in Fig. 9. Limiting magnitudes are slightly lower than in the 4T case, being respectively equal to 3, 6 and 8 when DIT = 0.5, 5 and 50 msec. This might be explained as follows: since the photon gain is brought by the two additional telescopes, the interferograms must now be sampled by much more pixels than in the 4T case (255 instead of 95, see Table 3), hence decreasing the irradiance on a single pixel and resulting in global performance loss. When seeing conditions are favorable however, the integration time may be increased when the OPD measurement error exceeds a certain threshold. An example of such an adaptive adjustment of DIT is illustrated in Fig. 10, showing that a magnitude 7 can be attained with a success ratio higher than 85% for a threshold value of 25 nm (it has been checked that higher thresholds correspond to non acceptable success ratios).

3.2.2 Coupling 4 ATs and 2 UTs

We finally study the case when 4 ATs and 2 UTs are coupled together. The obtained results are shown in Fig. 11 and are not significantly better in terms of limiting magnitude than in the previous case. A possible explanation is that the high difference in flux concentrated by the telescopes induces significant contrast losses (by a factor 20) on all MTF peaks associated to a couple of ATs. One may also note that the best results are obtained when

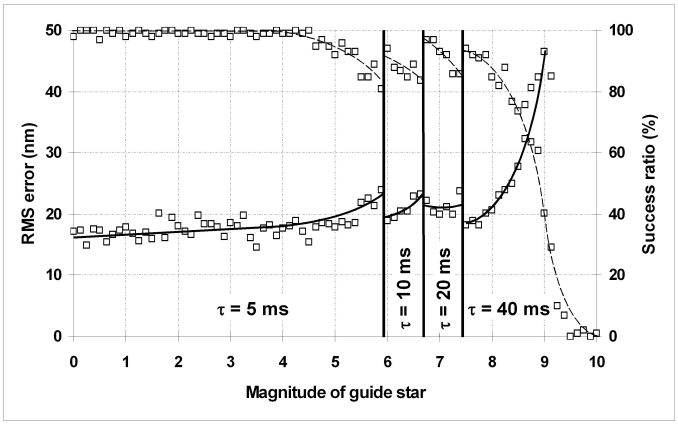

Figure 10. Adaptive adjustment of DIT in favorable seeing conditions for the 6T case and RON = 10 electrons/pixel. A magnitude 7 can be attained with a success ratio higher than 85%.

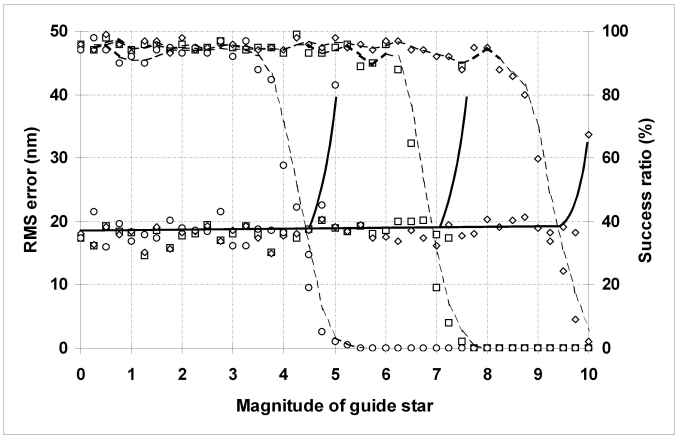

Figure 11. Same diagram as in Fig. 9 when coupling four ATs with two UTs.

the two UTs are coupled into the most distant waveguides of the IOC, *i.e.* number 1 and 6 on the bottom panel of Fig. 2.

4. POTENTIAL IMPROVEMENTS

Although most of physical parameters of the whole system have been carefully optimized in the frame of this Phase A study (including the data reduction procedure and particularly phase extraction and CPD algorithms), a few points leading to potential improvements remain to be investigated, such as the three following ones:

- Some optical parameters of the fringe tracker, and particularly the number n_P of pixels sampling the interferograms could be refined in order to better fit the Hawaii 2RG detector requirements and to achieve further gain in limiting magnitude (a goal of +1 seems to be reasonable).
- As demonstrated in this study, the phase extraction procedure with the current implementation of the CPD algorithm leads to a very high precision (almost 10 nm) but as soon as noise increases, to an insufficient success rate. A more robust determination with lower accuracy is possible but has not yet been implemented. Here another gain of one magnitude is to be expected.

- We also have to assess the performance of the whole system on partially resolved guide stars, when their visibility factors $V_{n,n'}$ become significantly lower than unity.

5. CONCLUSION

A multi-axial integrated optics solution associated with fringe dispersion and Chromatic Phase Diversity techniques has been studied in the perspective of POPS, a second-generation fringe tracker proposed to ESO for the Very Large Telescope Interferometer. We have depicted the foreseen design for optics, mechanics, detection system and data reduction software, and built a realistic simulation model of the whole system in order to evaluate its ultimate performance in terms of group and phase delay measurement accuracy, capture range and limiting magnitude. The numerical results demonstrate that a multi-axial IOC has the ability to fulfil most of the new-generation fringe tracker requirements, except in cophasing mode when using the currently selected detector. The proposed design has the ability to combine either four or six telescopes and shows some interesting and somewhat unusual properties such as accurate OPD measurements over a wide range of piston errors, good performance in linearity and immunity to phase jumps. It was found that the system can operate with the same measurement quality in both the phase delay and group delay modes, provided that the detector can achieve faster read-out rates. Since the contrasts between all telescope pairs are measured simultaneously, it is also possible to extract information on photometric variations affecting each individual telescope for monitoring purpose.

REFERENCES

[1] Tarmoul, N., Mourard, D., Hénault, F., Clausse, J.-M., Girard, P., Marcotto, A., Mauclert, N., Spang, A., Rabbia, Y., and Roussel, A., "Implementation of the Chromatic Phase Diversity method on the SIRIUS test bench: Results and performances of this cophasing method," *Proc. of SPIE* **7734** (2010).

[2] Koechlin, L., Lawson, P., Mourard, D., Blazit, A., Bonneau, D., Morand, F., Stee, P., Tallon-Bosc, I., and Vakili, F., "Dispersed fringe tracking with the multi-r_0 apertures of the Grand Interféromètre à 2 Télescopes," *Applied Optics* **35**, 3002–3019 (1996).

[3] Borkowski, V., Labeyrie, A., Martinache, F., and Peterson, D., "Sensitivity of a dispersed-speckles piston sensor for multi-aperture interferometers and hypertelescopes," *Astron. Astrophys.* **429**, 747–753 (2005).

[4] LAOG, "2gft low level specifications," *Internal documentation* (2010).

[5] Malbet, F., Kern, P., Schanen-Duport, I., Berger, J.-P., Rousselet-Perraut, K., and Benech, P., "Integrated optics for astronomical interferometry. i. concept and astronomical applications," *Astron. Astrophys. Suppl. Ser.* **138**, 135–145 (1999).

[6] Berger, J., Benech, P., Schanen-Duport, I., Maury, G., Malbet, F., and Reynaud, F., "Combining up to eight telescope beams in a single chip," *Proc. of SPIE* **4006**, 986–995 (2000).

[7] Nannini, M., Nerin, P., Benech, P., and Schanen-Duport, I., "Multiaxial beam combiner for optical coherence tomography," *Optical Engineering* **42**, 75–79 (2003).

[8] Lebouquin, J., Berger, J., Labeye, P. R., Tatulli, E., Malbet, F., Rousselet-Perraut, K., and Kern, P. Y., "Comparison of integrated optics concepts for a near-infrared multi-telescope beam combiner," *Proc. of SPIE* , 1362–+ (2004).

[9] Labeye, P., "Composants optiques intgrs pour l'interfromtrie astronomique," *PhD Thesis* (2008).

[10] Paxman, R. G. and Fienup, J. R., "Optical misalignment sensing and image reconstruction using phase diversity," *Journal of the Optical Society of America A* **5**, 914–923 (1988).

[11] Hénault, F., "Conceptual design of a phase-shifting telescope-interferometer," *Optics Communications* **261**, 34–42 (2006).

[12] Tarmoul, N., Mourard, D., and Hénault, F., "Study of a new cophasing system for hypertelescopes," *Proc. of SPIE* **7013** (2008).

[13] Lofdahl, M. and Eriksson, H., "An algorithm for resolving 2π ambiguities in interferometric measurements by use of multiple wavelengths," *Optical Engineering* **40**, 984–990 (2001).